Nanophotonics-enabled solar membrane distillation for off-grid water purification

Pratiksha D. Dongare[a,b,c,d,1], Alessandro Alabastri[a,b,d,1], Seth Pedersen[d,e], Katherine R. Zodrow[d,e], Nathaniel J. Hogan[a,b,c], Oara Neumann[a,b,d], Jinjian Wu[d,e], Tianxiao Wang[e], Akshay Deshmukh[d,f], Menachem Elimelech[d,f], Qilin Li[d,e,2], Peter Nordlander[a,b,d,g], and Naomi J. Halas[a,b,d,g,h,2]

[a]Department of Electrical and Computer Engineering, Rice University, Houston, TX 77005; [b]Laboratory for Nanophotonics, Rice University, Houston, TX 77005; [c]Applied Physics Graduate Program, Rice University, Houston, TX 77005; [d]Nanosystems Engineering Research Center for Nanotechnology-Enabled Water Treatment (NEWT), Rice University, Houston, TX 77005; [e]Department of Civil and Environmental Engineering, Rice University, Houston, TX 77005; [f]Department of Chemical and Environmental Engineering, Yale University, New Haven, CT 06520-8286; [g]Department of Physics and Astronomy, Rice University, Houston, TX 77005; and [h]Department of Chemistry, Rice University, Houston, TX 77005

Contributed by Naomi J. Halas, May 16, 2017 (sent for review February 2, 2017; reviewed by Svetlana V. Boriskina and Amy Childress)

With more than a billion people lacking accessible drinking water, there is a critical need to convert nonpotable sources such as seawater to water suitable for human use. However, energy requirements of desalination plants account for half their operating costs, so alternative, lower energy approaches are equally critical. Membrane distillation (MD) has shown potential due to its low operating temperature and pressure requirements, but the requirement of heating the input water makes it energy intensive. Here, we demonstrate nanophotonics-enabled solar membrane distillation (NESMD), where highly localized photothermal heating induced by solar illumination alone drives the distillation process, entirely eliminating the requirement of heating the input water. Unlike MD, NESMD can be scaled to larger systems and shows increased efficiencies with decreased input flow velocities. Along with its increased efficiency at higher ambient temperatures, these properties all point to NESMD as a promising solution for household- or community-scale desalination.

solar | photothermal | desalination | carbon black | nanophotonics

Four billion people around the world face at least 1 month of water scarcity every year (1, 2). To meet increasing water demand, it has become necessary to exploit saline water, abundant in the ocean and in brackish aquifers, and convert it to potable water (3, 4). Presently, there are more than 18,000 water desalination plants operating in 150 countries, producing 86.8×10^6 m^3 of water per day, enough for 300 million people (5, 6). The annual energy consumed by these plants is nominally 75 TWh, accounting for 50% of their operating costs (7–9) and 0.4% of the world electric power consumption (10). The possibility of directly using renewable energy would reduce this highly demanding cost of operation and make affordable clean water more accessible around the world.

Many of the current desalination techniques involve phase change, and thus are inherently energy intensive. Among these, membrane distillation (MD) has gained recent attention because it can distill water at lower temperatures than conventional distillation (i.e., boiling) and lower pressures than reverse osmosis (RO) (11–16). In the conventional direct-contact MD process, hot saline water (feed) and cold purified water (distillate) flow on opposite sides of a hydrophobic membrane (Fig. 1*A*). The temperature difference between the two flows produces a vapor pressure difference across the membrane, leading to (salt-free) water vapor transporting through the membrane from the warmer feed to the colder distillate, where it condenses. However, MD suffers from several inherent limitations. Heat transfer reduces the cross-membrane temperature difference, resulting in lower vapor flux across the membrane and thus lower efficiency. This temperature difference is further decreased along the length of the membrane module, resulting in a maximal usable length of a single module.

When no recirculation or heat recovery is used, energy is also lost when hot feed water exits the membrane module. Heating the volume of feed water by conventional solar methods before its flow through the module suffers these same inherent limitations (17–21). Localized heating in the feed channel can be achieved by integrating MD into industrial processes (22) or by using a solar absorber plate above the feed channel (23) to provide supplementary heating along the module length, but such a system is still limited by an inherent reduction in cross-membrane temperature difference due to heat transfer, for example, temperature polarization. Localized heating at the surface of the feed membrane interface (24–26) can provide an effective solution to overcome these challenges. In this work, we demonstrate nanophotonics-enabled solar membrane distillation (NESMD), where membrane distillation is based on direct, localized solar heating of a nanoparticle (NP)-infused membrane. We address the challenges of module scalability with experimental and theoretical analysis for a wide range of NESMD working conditions.

Here, we demonstrate direct solar distillation driven by NP-mediated photothermal heating in a MD geometry (Fig. 1*B*). This process is based on the highly efficient, highly localized photothermal heating (27–30) induced by solar illumination of broadband light-absorbing NPs, here embedded within the surface layer of the distillation membrane. The localized heating induces vaporization of the feed water, which subsequently condenses on the distillate side of the membrane. The localized solar photothermal heating process replaces the need to heat the entire volume of feed water by external means, eliminating the inherent efficiency limitations and substantial power requirements of the conventional MD

Significance

Current desalination technologies provide solutions to the increasing water demands of the planet but require substantial electric energy, limiting their sustainable use where conventional power infrastructure may be unavailable. Here, we report a direct solar method for desalination that utilizes nanoparticle-assisted solar vaporization in a membrane distillation geometry. This scalable process is capable of providing sufficient clean water for family use in a compact footprint, potentially for off-grid desalination at remote locations.

Author contributions: Q.L., P.N., and N. J. Halas designed research; P.D.D., A.A., S.P., K.R.Z., N. J. Hogan, O.N., and J.W. performed research; T.W., A.D., and M.E. contributed new reagents/analytic tools; P.D.D., A.A., and S.P. analyzed data; and P.D.D., A.A., S.P., K.R.Z., and N. J. Halas wrote the paper.

Reviewers: S.V.B., Massachusetts Institute of Technology; and A.C., University of Southern California.

Conflict of interest statement: A patent was filed on the NESMD process. This patent is pending.

Freely available online through the PNAS open access option.

[1]P.D.D. and A.A. contributed equally to this work.

[2]To whom correspondence may be addressed. Email: qilin.li@rice.edu or halas@rice.edu.

This article contains supporting information online at www.pnas.org/lookup/suppl/doi:10.1073/pnas.1701835114/-/DCSupplemental.

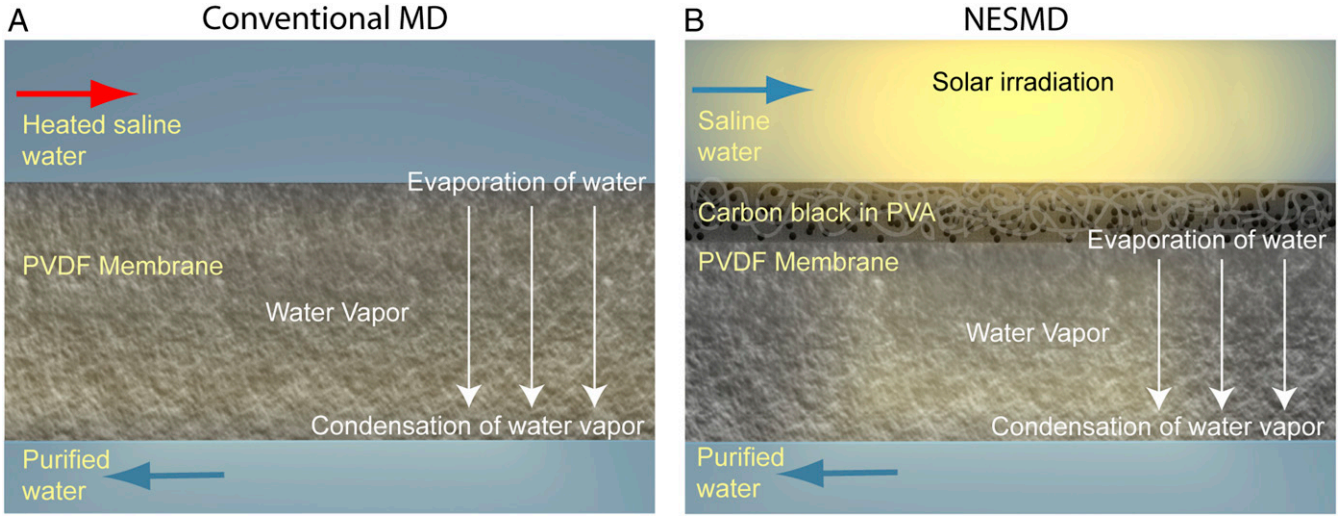

Fig. 1. Comparison of conventional membrane distillation (MD) and nanophotonics-enabled solar membrane distillation (NESMD). (*A*) In MD, heated saline (input) water and ambient temperature distillate water flow on each side of a PVDF membrane. The temperature difference generates a vapor pressure difference across the membrane, resulting in evaporation from the feed–membrane interface to condensation at the distillate–membrane interface. Nonvolatile contaminants do not evaporate and are therefore not present in the distillate. (*B*) In NESMD, light-absorbing (CB) NPs are embedded in an electrospun PVA layer deposited on a PVDF membrane. Upon solar illumination, the CB-laden membrane layer generates an elevated vapor pressure with no additional heat source. Water vapor condenses at the distillate–membrane interface.

process. Using a small-scale experimental NESMD module, we obtained a flux of over 5.38 kg/(m^2·h) with a solar efficiency of over 20% and greater than 99.5% salt rejection under focused solar illumination. Comparing NESMD to conventional MD reveals dramatic differences between the two processes, where unlike MD, NESMD appears readily scalable to larger geometries with increased efficiencies under higher ambient temperature conditions (40 °C). These characteristics point to NESMD as a highly promising potential off-grid desalination technology.

The photothermal membrane central to NESMD is a bilayer structure consisting of a relatively thin (25 μm), optically absorbing, porous, hydrophilic [polyvinyl alcohol (PVA)] coating deposited onto a commercial polyvinylidene fluoride (PVDF) membrane (0.2-μm nominal pore size; Pall Corporation) (Fig. 2*A*). Carbon black (CB) NPs (Cabot Corporation) with a broadband absorption over the entire solar spectrum (Fig. 2*E* and Fig. S1*B*) were dispersed into the PVA solution. Following a pretreatment by polydopamine to ensure adhesion, the PVA solution was electrospun onto the PVDF membrane, forming a network of CB-laden PVA nanofibers (Fig. 2 *A* and *F*, *Inset*).

The optical properties of the CB-laden bilayer photothermal membrane were characterized to determine an optimal concentration range of CB absorbers to serve as a heat source for NESMD (Fig. 2). The absorption efficiency and spatial distribution of absorbed energy together determine the heat source density, which dictates the solar photothermal temperature

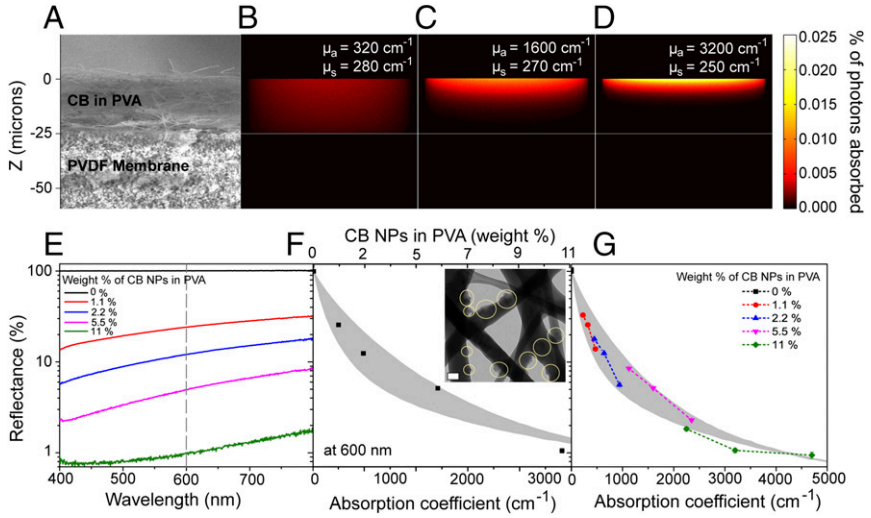

Fig. 2. Optical characterization of the photothermal membrane. (*A*) SEM image of the cross-section of the bilayer membrane. (*B–D*) Spatial photon absorption distributions in bilayer membrane as a function of CB concentration (wt%), corresponding to the dimensions shown in *A*. (*B*) 1.1 wt%; (*C*) 5.5 wt%; (*D*) 11 wt%. (*E*) Experimentally measured diffuse reflectance spectra for a photothermal membrane with varying CB concentrations. (*F*) Experimental (black squares) and theoretical (gray area) reflectance at 600 nm as a function of CB concentration. (*Inset*) Transmission electron micrograph (TEM) of CB-laden PVA coating of the bilayer membrane. (*G*) Reflectance versus absorption coefficient for varying CB concentrations in PVA at the wavelengths 800, 600, and 400 nm (*Left* to *Right*).

increase and thus the water vapor flux through the membrane. Because the CB-laden membrane is a medium that is both strongly optically scattering and absorbing, theoretical calculations using a Monte Carlo photon transport method were necessary to accurately describe the membrane's utility as a photodriven heat source (27). The calculated distribution of absorbed photons (Fig. 2 *B–D*) were compared with diffuse reflectance spectral measurements (Fig. 2*E*) of the bilayer membrane for a range of CB concentrations. Increased CB concentrations in the photothermal layer induce larger absorption coefficients in this region, resulting in more localized light absorption within this layer. The diffuse reflectance at 600 nm for membranes within a range of CB concentrations (Fig. 2*F*) shows a decreasing reflectance for increasing CB concentrations (top axis). Light transport simulations using the corresponding values of μ_a were performed for photothermal coatings of varying thicknesses of 25 ± 7 μm (SD) (Fig. 2*F*, shaded gray region). Agreement between the experimental diffuse reflectance measurements and the simulations provides an accurate relationship between the absorption coefficient, μ_a, and the concentration of CB NPs in the absorbing membrane layer at 600 nm. This combination of experimental measurements and theoretical simulations was extended across the visible spectrum (Fig. 2*G*), where data were obtained at 800, 600, and 400 nm and compared with theoretical simulations. The light absorption measurements and absorption coefficients obtained here were used to select an optimum CB concentration for the bilayer membrane (5.5 wt%). These values were used as input to a finite-element method (FEM)-based 3D model (COMSOL 5.2) developed to describe the coupled heat, fluid, and mass transfer processes in the NESMD system and in its comparison with MD (31, 32). Design flexibility and freedom in the choice of operational parameters allow analysis of NESMD and MD at different scales. This theoretical model is predictive and does not require calibration. Values of all of the physical parameters used in the simulations are obtained either from literature (14, 33) or experimental conditions (*Supporting Information*).

The NESMD system (Fig. 3*A* and Figs. S2 and S3) was tested outdoors in Houston, Texas (United States) (29.7604°N), where the measured average solar intensity was nominally 0.7 kW/m^2 (*Supporting Information*). The active area of illumination was a 3.3 × 6.8-cm window exposing the feed side of the membrane. Both the feed and distillate reservoirs were immersed in an ice bath and the system was covered with reflective insulation; however, a 3–5 °C temperature difference remained between the feed and distillate inlets due to sunlight irradiation on the system and heat loss to the ambient environment. The NESMD system stabilized at slightly different feed and distillate temperatures (in the range of 14–20 °C), remaining constant to within ±1 °C throughout the measurements. Accounting for all photothermal and thermal factors, the distillate flux from the NESMD system has three contributions:

$$J_{Total} = J_{NP} + J_{MD} + J_{res}. \quad [1]$$

Here, J_{Total} is the total measured flux from the photothermal membrane with NPs upon illumination; J_{NP} is the flux due to localized heating by CB NPs; J_{MD} is the flux due to experimental temperature difference between the bulk feed and distillate streams; J_{res} is the flux due to residual heating in the system upon illumination. To distinguish these different contributions we have performed specific measurements, as explained below.

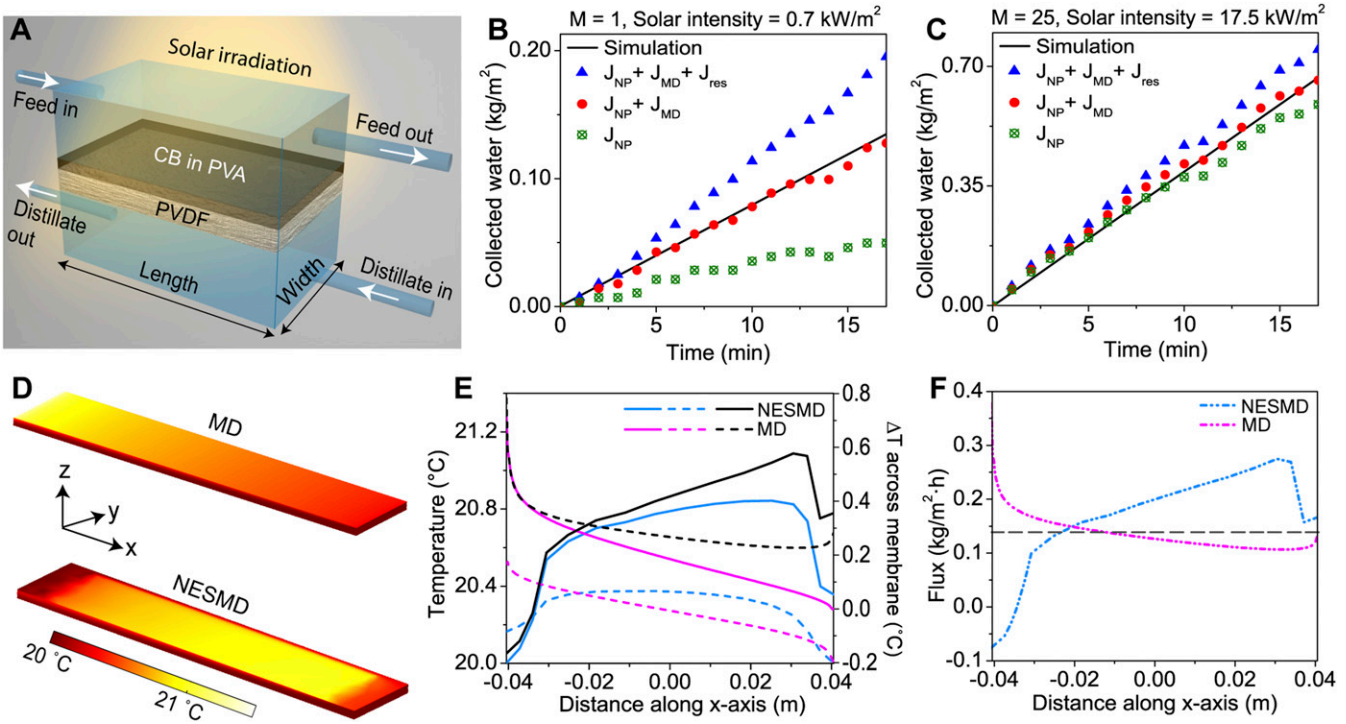

Fig. 3. Comparison of outside solar experiments and for NESMD and MD. (*A*) Schematic of the NESMD module. (*B*) Purified water flux under unfocused illumination. (*C*) Flux obtained under 25× focused solar illumination. Blue triangles: experimental distillate flux J_{Total}. Black line: theory. Red circles: experimental flux minus measured the experimental flux from illuminated membrane without CB NPs (residual heating effects; $J_{Total} - J_{res}$). Green circles: experimental flux due only to localized photothermal heating; $J_{NP} = J_{Total} - J_{res} - J_{MD}$. (*D*) Calculated temperature distributions at the membrane surface for MD (*Top*) and NESMD (*Bottom*). The feed inlet temperature is 20 °C in NESMD and 21.3 °C in MD, corresponding to same input energy in NESMD (solar) and MD, with a distillate temperature of 20 °C for both processes. (*E*) Theoretical temperature profile at the feed (solid) and distillate (dotted) sides of the membrane for NESMD (blue) and MD (magenta) for same conditions as in *D*. Theoretical temperature drop (right axis) across the membrane (black) for NESMD (solid) and MD (dotted). (*F*) Calculated flux profile for NESMD at 0.7 kW/m^2 solar illumination (dot-dashed blue) and MD (dot-dashed magenta) for temperatures specified in *C*. Dashed gray line: average flux.

We obtain J_{Total} by measuring the distillate flux through the NESMD system upon illumination. It is shown with blue triangles in Fig. 3 *B* and *C* for no magnification, and for 25× magnification, respectively. The flux through the NESMD module without illumination gives us J_{MD}, as designated with hollow black diamonds in Fig. S4. To measure J_{res}, we first performed measurements in exactly the same experimental setup using a control membrane containing no CB NPs. The flux from this membrane upon illumination comes from $(J_{MD}+J_{res})$ (shown with violet diamonds in Fig. S4). Second, we measure the flux through the same membrane without illumination to obtain J_{MD} only (shown with hollow gray circles in Fig. S4). The difference between these two fluxes gives J_{res} (shown with navy-blue stars in Fig. S4 *A* and *B* for no magnification and 25× magnification, respectively). Subtracting alternatively J_{res} and $J_{res}+J_{MD}$ from J_{Total} gives us $(J_{NP}+J_{MD})$ (solid red circles) and J_{NP} (hollow green circles), respectively. Both nonmagnified and 25× magnified cases are shown in Fig. 3 *B* and *C*, respectively. Although in the experiment the illumination area does not cover the whole device surface, all of the flux calculations here use the total module area to evaluate the contribution from each flux component. Upon quantification of each flux, the values of J_{NP} normalized to the illumination window areas compared with other fluxes are shown in Fig. S5.

The purified water flux from saline feed water (with a salt rejection rate of >99.5%; *Supporting Information*) is shown for unfocused (Fig. 3*B*) and focused (Fig. 3*C*) illumination conditions and compared with our theoretical model for NESMD. For unfocused solar illumination (Fig. 3*B*), the experimental distillate flux exceeds theoretical predictions; however, there is good agreement between theoretical and experimental distillate flux once the contribution made by residual solar heating (J_{res}), not included in the model, is accounted for. In this low-intensity case, even the residual heating inherent in the system (J_{MD}) (Fig. S4) contributes significantly to the experimental distillate flux; when this is also removed, we obtain the distillate flux due to localized CB NP heating alone (J_{NP}). In contrast, for the case of 25× focused illumination (Fig. 3*C*), localized photothermal heating provides the dominant contribution to the distillate flux in this system.

The energy efficiency of NESMD is determined by evaluating the energy requirement of producing the distillate flux by localized photothermal heating (J_{NP}) relative to the incident solar power. For the unfocused case, the photothermal distillate flux is 0.22 kg/(m^2·h) (Fig. S5*C*). Given the water evaporation enthalpy of 2,454 kJ/kg (34), the minimum power needed to sustain this evaporation rate is 0.337 W. The total absorbed power through the illuminated area of the window (3.3 cm × 6.8 cm) is 1.571 W, corresponding to an efficiency of 21.45%. For 25× focusing (Fig. 3*C*), the solar distillation process is 21.0% efficient (assuming an illumination spot of 3.3 × 3.3 cm on the membrane, in agreement with experimental focusing geometry).

The accuracy of the theoretical model for NESMD allows us to examine the geometry and size-dependent aspects of this process, and to compare it to conventional MD. These studies reveal stark differences between the two processes. For example, the temperature along the length of the membrane is examined for both processes (Fig. 3 *D* and *E*). Here, we compare NESMD under unfocused illumination conditions with MD. In the MD case, a temperature difference of 1.33 °C between the feed and the distillate corresponds to the same power input as the illumination intensity for NESMD (1.57 W). The two processes have entirely different temperature profiles: for MD, where the feed is heated externally, the feed temperature is highest at the feed inlet, which is also the point of largest temperature difference between feed and distillate (Fig. 3*E*). In contrast, for NESMD, where the temperature difference between feed and distillate is generated by solar illumination, the feed temperature increases along the feed flow channel. In this case, the largest temperature difference is generated close to the feed outlet. The distillate flux generated along the flow channel follows this temperature dependence in both cases (Fig. 3*F*). From these results, we project that increasing the size of an NESMD unit should increase its distillate flux, in contrast to MD, where scale-up beyond a certain point would not correspond to an increased purified water output.

Further comparisons of NESMD and MD reveal additional opposing trends between the two processes. Another key parameter of purification systems is feed velocity. The calculated distillate fluxes for feed velocities ranging between 0.0032 cm/s (0.1 mL/min) and 3.2 cm/s (100 mL/min) in a bench-scale device (8.1 × 3.5 cm) for both unfocused NESMD and MD are shown in Fig. 4*A*. For simplicity, the illuminated area is now considered to be equal to the total area of the device. For NESMD, temperatures of the feed and distillate at the inlet are equal at 20 °C, and the velocity of the distillate is set to 136 mL/min (the experimental value). For MD, the distillate inlet temperature was the same, and the feed temperature was chosen to match the power input for NESMD. The dependence of distillate flux on feed flow velocity is opposite for NESMD and MD, although both methods provide more flux with lower membrane thermal conductivity and higher diffusion coefficient (corresponding to larger membrane porosity) (Fig. S6). NESMD is most efficient at lower feed flow rates, whereas MD flux is maximized only at higher flow rates. Both trends can be understood considering the temperature gradient across the membrane. For NESMD, slower feed velocities allow time for a larger temperature gradient to form between the feed and distillate sides of the membrane, resulting in a larger distillate flux. For MD, where the feed is heated before entry into the module, higher feed velocities reduce heat loss for the feed flow along the membrane. The efficient operation of the NESMD for modest flow velocities would be a significant advantage over MD in off-grid locations because solar-driven water pumps could be used. In addition, significantly less energy would be required for brine recirculation, which can be an important factor in the overall energy use of conventional MD (35).

We also observe striking differences between the average distillate flux for NESMD and MD as a function of module length and width (Fig. 4*B*), due to the differences in heat transfer between these two processes. The flux produced at larger lengths and widths increases in the NESMD case while decreasing to nearly zero for the largest membranes for MD at a fixed feed inlet temperature (21.67 °C, corresponding to the input power for the NESMD system under unfocused conditions). For the case of constant feed flow (17 mL/min, the experimental value), increasing the width of NESMD and MD corresponds to a reduction in flow velocity; thus, increasing the width of the system results in increased distillate flux for NESMD but decreased flux for MD (Fig. 4*B*). In MD, the increase in length increases the heat loss from feed to distillate side, resulting in a progressively reduced temperature difference across the membrane and thus lower fluxes. When the temperature difference between the feed and distillate sides of the membrane becomes negligible, the vapor transport vanishes and the effective fraction of active area of the device is reduced. In NESMD, however, the membrane remains active for longer module lengths (Fig. 4*C* and Fig. S7). A direct efficiency comparison of MD and NESMD shows that NESMD has consistently higher efficiencies than MD (Figs. S8 and S9) for the module lengths considered here (*Supporting Information*).

Another important factor that influences NESMD performance is the ambient operating temperature (Fig. 4*D* and Fig. S10). Here, the flux dependence on ambient temperature is determined for both a bench-scale (black, 8.1 × 3.48 cm) and pilot-scale (red, 100 × 10 cm) device under unfocused conditions. The temperature difference between the feed and the distillate without illumination is zero in all cases. In both cases, the performance significantly improves (more than two times) when the ambient temperature is increased from 10 to 40 °C. Higher ambient temperatures also favor the larger-dimensioned system. At the highest temperature, the flux for the pilot-scale device is 0.55 kg/(m^2·h), which

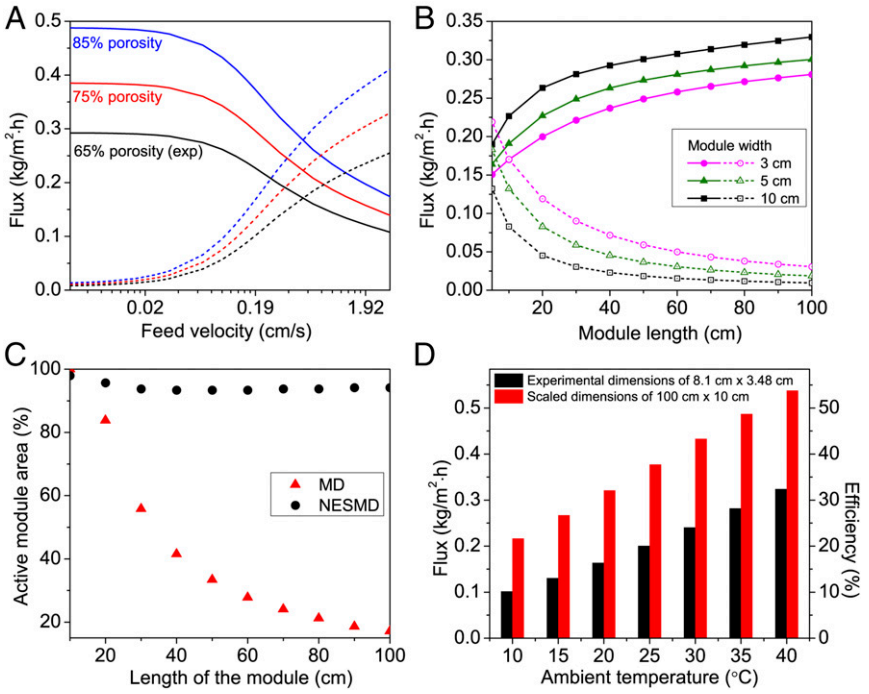

Fig. 4. Analysis of performance and scalability of NESMD. (*A*) Flux dependence on the feed velocity (log scale) for NESMD (solid lines) and MD (dashed lines) for different PVDF membrane porosities of 65% (black, equal to experimental value), 75% (red), and 85% (blue). Distillate flow is 136 mL/min (equal to the experimental value). All parameters are the same as in Fig. 3 except the illumination area, which is assumed here to be equal to the area of the device. (*B*) Flux dependence on cell length for NESMD (solid lines) and MD (dashed lines) for different cell widths: 3 cm (magenta), 5 cm (green), and 10 cm (black). (*C*) Active membrane area (area with positive temperature gradient across membrane) for lengths from 10 to 100 cm and a 10-cm width for NESMD (black circles) and MD (red triangles). (*D*) Flux dependence on ambient temperature (same temperature on feed and distillate side) for NESMD for two different cell sizes: 3.5 × 8.1 cm (black, same as experimental unit) and 10 × 100 cm (red). The feed flow is 17 mL/min, and the thermal conductivity of the membrane is taken from Fig. S6 for experimental porosity of 65%.

corresponds to a solar energy efficiency of 53.8%. With peak temperatures of ∼35 °C, a water purification rate of ∼0.5 kg/(m^2·h), and an active area of ∼1 × 1 m, an NESMD system without any form of heat recovery would produce ∼4 L/day under less than 1 sun (700 W/m^2) illumination, with 8 h of sunlight in the summer. This production rate meets the basic drinking water requirements for two persons (36).

The performance of NESMD system can be further increased by incorporating heat recovery by recirculating feed output back to feed input. This recirculation not only will allow use of the heat lost in the form of the heated feed output of NESMD but also will increase the overall water recovery of the system by minimizing brine production from the system. This would increase the water flux and improve overall energy efficiency because the net energy consumption per unit volume of purified water produced will be reduced. Heat recovery mechanisms proposed for MD systems to use distillate heat generated from condensation and conductive heat transfer through the membrane via heat exchange to preheat the feed (37) should work equally well for NESMD. It should also be possible to use vacuum MD or air-gap MD geometry to minimize heating on the distillate side. In terms of thermodynamic performance limits, thermal processes such as NESMD operate further from the theoretical second law reversible limit than RO (38). However, the ability of NESMD to directly harness solar energy for desalination is favorable compared with the need to produce high-grade electrical energy for RO, which is limited by low-efficiency photovoltaic conversion when solar panels are used.

This discovery, the integration of photothermal heating capabilities within a water purification membrane for direct, solar-driven desalination, opens opportunities in water purification technologies. Unlike MD, NESMD benefits from increases in scale and in ambient operating temperatures, and requires only modest flow requirements for optimal distillate conversion. Further opportunities in developing light-harvesting capabilities, higher performance photothermal membranes, and flow geometries are likely to enhance performance even further. However, the NESMD system described here, which can be realized as a "solar desalination panel," has direct, practical applications for scalable, solar-driven, and cost-effective desalination.

Materials and Methods

Fabrication of the Photothermal Membrane. Before applying the photothermal coating, one side of the PVDF membrane was contacted with a 2 mg/mL dopamine hydrochloride (Sigma) solution in 0.1 M Tris·HCl (pH 8.5) for 15 min. The polydopamine layer formed aids in adhesion of the hydrophilic photothermal coating to the hydrophobic PVDF membrane. To prepare the electrospinning solution, functionalized CB NPs (Cabot Corporation) were first suspended in deionized water using probe sonication (Sonics Vibra-Cell; 35 W) for 10 min. Poly (vinyl alcohol), *N*-methyl-4(4′-formylstyryl)pyridinium methosulfate acetal (PVA-SbQ) (Polysciences) was then added to the suspension to yield a final PVA-SbQ concentration of 8.87%. The suspension was vortexed to evenly distribute the polymer and the CB. The CB concentration was varied from 0.1 to 1.0 wt% in the electrospinning solution, corresponding to 1.1–11 wt% in the PVA-SbQ polymer.

The electrospinning solution was loaded in a 3-mL syringe placed 10 cm away from the aluminum sheet metal collector plate, where the polydopamine-coated PVDF membrane was mounted. The syringe was advanced using a syringe pump (New Era Pump Systems; NE-1000) at the rate of 0.5 mL/min, and a 10-kV voltage was applied (Gamma High Voltage Research; ES50P-5W) between the syringe tip and the collector plate (39). After electrospinning for 3 h, the membrane was placed in a photoreactor (Luzchem; LZC-4V) equipped with 8 UV-A bulbs (Hitachi; FL8BL-B; peak emission at 352 nm) for 30 min to cross-link the styrylpyridinium groups (40). A beaker of water was placed inside the chamber to maintain the humidity level and prevent dehydration of the PVA.

Experimental Setup. NESMD experiments were carried out using a custom-built membrane distillation module (Fig. S3) in direct-contact mode. A schematic of the system and the actual setup is shown in Fig. S2. The membrane module consists of a 1-mm-thick quartz window with dimensions of 3.3 × 6.8 cm on the feed side to allow sunlight illumination. Flow channel

dimensions were 3.48 × 8.10 × 0.15 cm on both the feed and distillate sides. A 1-mm-thick polypropylene mesh spacer (McMaster; catalog no. 9265T49) was used on the distillate side, and a modified spacer with perpendicular mesh segments removed was used on the feed side to support the membrane while maintaining laminar flow. The cross-flow velocities in the feed and distillate channels were 0.54 cm/s (flow rate, 17 mL/min) and 4.34 cm/s (flow rate, 136 mL/min), respectively. The feed stream (saline stream) on the top of the membrane was a 1% NaCl (J. T. Baker) solution stored in a 500-mL Erlenmeyer flask, and deionized water (produced by a Barnstead E-Pure system and Milli-Q Integral; Millipore) was used for the distillate stream at the bottom of the membrane. We chose 1% salinity to mimic average salinity of brackish water, which is a main saline water supply used inland. To maintain stable temperatures on both sides of the membrane, the feed and distillate were cooled by 15-m-long chilling coils submerged in a shaded ice bath before entering the NESMD module. The feed and distillate were continuously circulated through the membrane module using peristaltic pumps (Masterflex L/S) in a countercurrent flow mode, where feed and distillate streams flow in opposite directions.

The insulated distillate reservoir was kept on a weighing balance (Denver Instruments; P402) connected to a computer equipped with data acquisition software (TAL Tech WinWedge). The increase in distillate mass was measured with the balance at 1-min intervals. A sketch of a vertical cross-section of the module is shown in Fig. 1*B*. An inline conductivity meter (Oakton pH/CON 510 series) was installed at the exit of the distillate channel to monitor the salinity of the distillate. Inlet and outlet temperatures for both the feed and distillate streams were measured using in-line thermometers (Traceable; no. 4351). For NEMD experiments with solar concentration, a 25.4 × 25.4 cm Fresnel lens was used to concentrate sunlight on the membrane surface by a factor of 25. The unconcentrated and concentrated solar intensities at the NESMD module surface were 0.7 and 17.5 $kW{\cdot}m^{-2}$, respectively (Thorlabs; S350C; Thermal Surface Absorber). We understand that the Fresnel lens used for solar concentration has optical losses; however, we use the incident power at the NESMD module surface as the input power for the efficiency calculations, as we are interested in the NESMD unit performance. All system components, except the membrane module, Fresnel lens, computer, and power meter were enclosed in an insulated box made of radiation barrier foam to prevent excessive solar heating of the system components (Fig. S3).

ACKNOWLEDGMENTS. This work was funded by the Nanoscale Science and Engineering Initiative of the NSF under NSF Award EEC-1449500, Air Force Office of Scientific Research Grant FA9550-15-1-0022, Robert A. Welch Foundation Grants C-1220 and C-1222, and J. Evans Attwell–Welch Fellowship L-C-0004.

1. Mekonnen MM, Hoekstra AY (2016) Four billion people facing severe water scarcity. *Sci Adv* 2:e1500323.
2. Service RF (2006) Desalination freshens up. *Science* 313:1088–1090.
3. Elimelech M, Phillip WA (2011) The future of seawater desalination: Energy, technology, and the environment. *Science* 333:712–717.
4. Werber JR, Osuji CO, Elimelech M (2016) Materials for next-generation desalination and water purification membranes. *Nat Rev Mater* 1:16018.
5. Bennett A (2013) 50th Anniversary: Desalination: 50 years of progress. *Filtr Sep* 50:32–39.
6. Anonymous (2011) IDA World Congress: Desalination market grows to meet global water needs. *Filtr Separat* 48:28–30.
7. Ghaffour N, Missimer TM, Amy GL (2013) Technical review and evaluation of the economics of water desalination: Current and future challenges for better water supply sustainability. *Desalination* 309:197–207.
8. Lapuente E (2012) Full cost in desalination. A case study of the Segura River Basin. *Desalination* 300:40–45.
9. Miller JE (2003) *Review of Water Resources and Desalination Technologies* (Sandia National Laboratory, Albuquerque, NM), Report SAND2003-0800, pp 3–54.
10. Renewable I, Agency E (2012) *Water Desalination Using Renewable Energy* (International Renewable Energy Agency, Masdar City, Abu Dhabi, United Arab Emirates).
11. Lawson KW, Lloyd DR (1997) Membrane distillation. *J Membr Sci* 124:1–25.
12. Cath TY, Adams VD, Childress AE (2004) Experimental study of desalination using direct contact membrane distillation: A new approach to flux enhancement. *J Membr Sci* 228:5–16.
13. Alkhudhiri A, Darwish N, Hilal N (2012) Membrane distillation: A comprehensive review. *Desalination* 287:2–18.
14. Gryta M (2012) Effectiveness of water desalination by membrane distillation process. *Membranes (Basel)* 2:415–429.
15. Camacho LM, et al. (2013) Advances in membrane distillation for water desalination and purification applications. *Water* 5:94–196.
16. Goh PS, Matsuura T, Ismail AF, Hilal N (2016) Recent trends in membranes and membrane processes for desalination. *Desalination* 391:43–60.
17. Koschikowski J, Wieghaus M, Rommel M (2003) Solar thermal driven desalination plants based on membrane distillation. *Water Sci Technol Water Supply* 3:49–55.
18. Ding Z, Liu L, El-Bourawi MS, Ma R (2005) Analysis of a solar-powered membrane distillation system. *Desalination* 172:27–40.
19. Mathioulakis E, Belessiotis V, Delyannis E (2007) Desalination by using alternative energy: Review and state-of-the-art. *Desalination* 203:346–365.
20. Chang H, Wang GB, Chen YH, Li CC, Chang CL (2010) Modeling and optimization of a solar driven membrane distillation desalination system. *Renew Energy* 35:2714–2722.
21. Qtaishat MR, Banat F (2013) Desalination by solar powered membrane distillation systems. *Desalination* 308:186–197.
22. Hausmann A, Sanciolo P, Vasiljevic T, Weeks M, Duke M (2012) Integration of membrane distillation into heat paths of industrial processes. *Chem Eng J* 211–212:378–387.
23. Chen TC, Ho CD (2010) Immediate assisted solar direct contact membrane distillation in saline water desalination. *J Membr Sci* 358:122–130.
24. Politano A, et al. (2017) Photothermal membrane distillation for seawater desalination. *Adv Mater* 29:1603504.
25. Summers EK, Lienhard V JH (2013) A novel solar-driven air gap membrane distillation system. *Desalination Water Treat* 51:1344–1351.
26. Summers EK, Lienhard V JH (2013) Experimental study of thermal performance in air gap membrane distillation systems, including the direct solar heating of membranes. *Desalination* 330:100–111.
27. Hogan NJ, et al. (2014) Nanoparticles heat through light localization. *Nano Lett* 14: 4640–4645.
28. Neumann O, et al. (2013) Solar vapor generation enabled by nanoparticles. *ACS Nano* 7:42–49.
29. Ghasemi H, et al. (2014) Solar steam generation by heat localization. *Nat Commun* 5: 4449.
30. Zhou L, et al. (2016) 3D self-assembly of aluminium nanoparticles for plasmon-enhanced solar desalination. *Nat Photonics* 10:393–398.
31. Tahvildari K, et al. (2016) Modeling and simulation of membrane separation process using computational fluid dynamics. *Arab J Chem* 9:72–78.
32. Shirazi MMA, Kargari A, Ismail AF, Matsuura T (2016) Computational fluid dynamic (CFD) opportunities applied to the membrane distillation process: State-of-the-art and perspectives. *Desalination* 377:73–90.
33. Stephan K, Laesecke A (1985) The thermal conductivity of fluid air. *J Phys Chem Ref Data* 14:227–234.
34. Woodward FI, Sheely JE (1983) *Principles and Measurements in Environmental Biology* (Butterworth-Heinemann Ltd, London).
35. Zou S, Yuan H, Childress A, He Z (2016) Energy consumption by recirculation: A missing parameter when evaluating forward osmosis. *Environ Sci Technol* 50:6827–6829.
36. Gleick P (1996) Basic water requirements for human activities: Meeting basic needs. *Water Int* 21:83–92.
37. Lin S, Yip NY, Elimelech M (2014) Direct contact membrane distillation with heat recovery: Thermodynamic insights from module scale modeling. *J Membr Sci* 453:498–515.
38. Mistry KH, et al. (2011) Entropy generation analysis of desalination technologies. *Entropy* 13:1829–1864.
39. Liu Y, Bolger B, Cahill PA, McGuinness GB (2009) Water resistance of photocrosslinked polyvinyl alcohol based fibers. *Mater Lett* 63:419–421.
40. Ichimura K (1987) Photocrosslinking behavior of poly (vinyl alcohol)s with pendent styrylpyridinium or styrylquinolinium groups. *Makromol Chem* 188:2973–2982.
41. Wang XQ, Mujumdar AS (2008) A review on nanofluids—Part I: Theoretical and numerical investigations. *Braz J Chem Eng* 25:613–630.
42. Buonomenna MG, et al. (2007) New PVDF membranes: The effect of plasma surface modification on retention in nanofiltration of aqueous solution containing organic compounds. *Water Res* 41:4309–4316.
43. Wang M, Pan N (2008) Predictions of effective physical properties of complex multiphase materials. *Mater Sci Eng Rep* 63:1–30.
44. Tjaden B, Cooper SJ, Brett DJ, Kramer D, Shearing PR (2016) On the origin and application of the Bruggeman correlation for analysing transport phenomena in electrochemical systems. *Curr Opin Chem Eng* 12:44–51.
45. Marrero TR, Mason EA (1972) Gaseous diffusion coefficients. *J Phys Chem Ref Data* 1:3–118.
46. Fasano M, et al. (2016) Interplay between hydrophilicity and surface barriers on water transport in zeolite membranes. *Nat Commun* 7:12762.
47. Comsol (2015) *Heat Transfer Module* (COMSOL AB, Stockholm, Sweden), pp 1–222.
48. Comsol (2015) *CFD Module User's Guide* (COMSOL AB, Stockholm, Sweden).
49. Griffiths E (1927) International critical tables of numerical data physics, chemistry and technology. *Nature* 119:735–738.
50. Stokes GG (1845) On the theories of the internal friction of fluids in motion, and of the equilibrium and motion of elastic solids. *Trans Cambridge Philos Soc* 8:287–319.
51. Ross RG, Andersson P, Backstrom G (1977) Thermal conductivity of nine solid phases of water. *High Temp High Press* 9:87–96.
52. Childs GE, Ericks LJ, Powell RL (1973) Thermal conductivity of solids at room temperature and below: A review and compilation of the literature. Available at digital.library.unt.edu/ark:/67531/metadc13173. Accessed May 31, 2017.
53. Fox RW, McDonald AT, Pritchard PJ (2004) *Introduction to Fluid Mechanics* (Wiley, New York), 6th Ed.
54. ASTM International (2012) *ASTM G173-03 - Standard Tables for Reference Solar Spectral Irradiances: Direct Normal and Hemispherical on 37° Tilted Surface* (ASTM International, West Conshohocken, PA).
55. Deacon EL (1974) Principles of environmental physics. *Agric Meteorol* 13:429–430.
56. Khayet M (2013) Solar desalination by membrane distillation: Dispersion in energy consumption analysis and water production costs (a review). *Desalination* 308:89–101.
57. Swaminathan J, Chung HW, Warsinger DM, Lienhard V JH (2016) Membrane distillation model based on heat exchanger theory and configuration comparison. *Appl Energy* 184:491–505.